Vibration-based hypervelocity impact identification and localization[*]

Jiao BAO[1], Lifu LIU[2], Jiuwen CAO[†‡2,3]

[1]Department of Computer Engineering, Chengdu Technological University, Chengdu 611730, China
[2]Machine Learning and I-health International Cooperation Base of Zhejiang Province,
Hangzhou Dianzi University, Hangzhou 310018, China
[3]Artificial Intelligence Institute, Hangzhou Dianzi University, Hangzhou 310018, China
[†]E-mail: jwcao@hdu.edu.cn

Abstract: Hypervelocity impact (HVI) vibration source identification and localization have found wide applications in many fields, such as manned spacecraft protection and machine tool collision damage detection and localization. In this paper, we study the synchrosqueezed transform (SST) algorithm and the texture color distribution (TCD) based HVI source identification and localization using impact images. The extracted SST and TCD image features are fused for HVI image representation. To achieve more accurate detection and localization, the optimal selective stitching features $OS_{SST+TCD}$ are obtained by correlating and evaluating the similarity between the sample label and each dimension of the features. Popular conventional classification and regression models are merged by voting and stacking to achieve the final detection and localization. To demonstrate the effectiveness of the proposed algorithm, the HVI data recorded from three kinds of high-speed bullet striking on an aluminum alloy plate is used for experimentation. The experimental results show that the proposed HVI identification and localization algorithm is more accurate than other algorithms. Finally, based on sensor distribution, an accurate four-circle centroid localization algorithm is developed for HVI source coordinate localization.

Key words: Ensemble learning; Synchrosqueezied transform; Gray-level co-occurrence matrix; Image entropy; Distance estimation

　　　　CLC number: TP391.4

1 Introduction

With the cumulative increase in human space activities, space environment is deteriorating, and a large number of various types of space debris, such as tiny meteor bodies, orbital debris particles, and spacecraft wreckage, are distributed in Earth's orbit

(Erickson, 2014; Millan et al., 2019; Wilson, 2019), as shown in Fig. 1. The hypervelocity impact (HVI) risk from space debris has become one of the main threats to space activities (Liou and Johnson, 2006; Witze, 2018). Due to the randomness of meteoroid/orbital debris (M/OD) impact events (Liou and Johnson, 2006), speed and size of the space debris are generally unknown, and the impact locations on manmade aircraft are usually difficult to determine accurately. Thus, accurate detection and localization of the HVI vibration source are significantly important in impact damage assessment, spacecraft protection, M/OD impact measurement, etc.

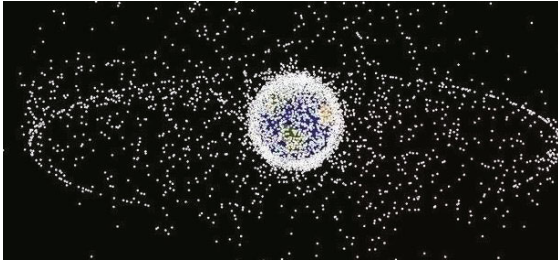Surface vibrations can capture information such

Fig. 1 The current status of the space environment around Earth in 2019

as the speed and quality of space debris during the collision, and also contain the impact location information. The vibrations generated by collisions are non-stationary signals; in the past, the mainstream in non-stationary signal analysis has been the time-frequency-based methods, including short-time Fourier transform (STFT) (Qian and Chen, 1999; Chan et al., 2001; Monti et al., 2002; Cohen, 2013), wavelet transform (WT) (Mallat, 1989; Auger and Flandrin, 1995), Gabor transform (Daubechies and Maes, 1996), and Wigner-Ville distribution (WVD) (Flandrin et al., 2013). Linear time-frequency and time-scale analysis is also popular for non-stationary signals or deterministic signals with varying frequency content. In particular, multicomponent signals, i.e., superpositions of amplitude- and frequency-modulated (AM-FM) waves, were comprehensively studied in Torrence and Compo (1998). Due to the Heisenberg uncertainty principle, STFT, Gabor transform, and WT are generally not suitable (Daubechies, 1990). Compared to other time-frequency distributions, WVD has the simplest form and good time-frequency resolution (Stankovic et al., 2014), and the smoothing pseudo WVD (SPWVD) can successfully eliminate the intersection of signal intervals and coherent items in the time-increasing direction (Önsay and Haddow, 1993). When STFT is applied to estimate the instantaneous frequency of the FM signals, it usually suffers from relatively low estimation accuracy. In Almeida (1994) and Bai et al. (2012), the fractional Fourier transform (FRFT) (Flandrin et al., 2013) was introduced into the short-term fractional Fourier transform (STFRFT) for non-stationary signal analysis. Using the FRFT to capture highly time-frequency aggregated linear frequency modulation signals can make it easier to capture the high time-frequency resolution results of nonlinear FM signals (Tao et al., 2010).

The synchrosqueezed transform (SST) is a method of redistributing the coefficients in the time-frequency matrix, and its purpose is to perform sharpening while maintaining reversibility. At present, there are mainly two novel time-frequency transform methods based on SST, the Fourier synchrosqueezd transform (FSST) (Yang et al., 2008; Thakur et al., 2013) and the wavelet synchrosqueezd transform (WSST) (Ghosh et al., 2019). The representative transform methods, i.e., FSST, WSST, SPWVD, STFRFT, have been widely used in nonstationary signal analysis (Yang et al., 2008) due to their excellent time-frequency resolution, accurate specific frequency band extraction, and statistics characterization. Based on these methods, advanced features have been developed to enhance the performance (Yang et al., 2008). In HVI signal analysis, the effect of the impact angle of the projectile has been investigated in Pierazzo and Melosh (2000). The three-dimensional hydrocode simulations presented in the paper revealed that in oblique impacts, the distribution of shock pressure inside the projectile was highly complex and had only bilateral symmetry. The HVI flash decay rate was studied in Anderson and Schultz (2006), where the decay rate was highly dependent on the initial condition, especially for the target material. The effects of HVI on two novel composite materials were studied in Huang et al. (2016, 2020). In Liu et al. (2019), a novel HVI source detection and localization method based on the multi-scale discrete wavelet transform (MDWT) and the kernel extreme learning machine (KELM) (Cao et al., 2019, 2020; Wang et al., 2020) was developed. A novel HVI damage evaluation method was developed by Yin et al. (2019), where an active infrared thermal wave image detection technology with multi-objective feature extraction optimization (MO-FEO) was proposed for HVI damage evaluation.

To create better descriptions of HVI signals, we propose several advanced features based on the spectrogram of vibrations. After the SST, the spectrogram contains rich texture and color distribution information (Materka and Strzelecki, 1998), which can be extracted for HVI signal representation. Particularly, the gray-level co-occurrence matrix (GLCM) (Mamli and Kalbkhani, 2019) and the image entropy can reflect the characteristics of the HVI signal time-frequency statistics (Mirzapour and Ghassemian,

2013). In this study, SST is first obtained and then texture color distribution (TCD) features on SST are extracted. Then, based on the correlation and similarity between the HVI source label and each dimension feature, feature selection is performed and the optimal selective stitching features $\mathrm{OS_{SST+TCD}}$ are obtained.

With the obtained $\mathrm{OS_{SST+TCD}}$ vibration features, an ensemble learning model is developed for HVI source classification and impact distance regression. Two strategies, voting and stacking, are applied and studied in ensemble learning. Popular conventional learning models, including k-nearest neighbor (kNN), decision trees (DT), support vector machine (SVM), logistic regression (LR), multi-layer perceptron (MLP), random forest (RF), extra trees (ET), AdaBoost, and gradient boosting (GB), are adopted as the bases of the ensemble learning method. With accurate HVI source classification and impact distance estimation, a four-circle centroid localization (FCL) algorithm is developed to perform HVI source localization based on sensor position distributions. The performance of the proposed method is validated using the real recorded HVI vibration signals generated by the impact of three kinds of high-speed bullets striking an aluminum alloy plate.

The contributions of the paper are three-fold: (1) the novel features $\mathrm{OS_{SST+TCD}}$, based on the SST and its texture color features, proposed to represent HVI vibrations; (2) an ensemble learning model based on voting and stacking generalization strategies is proposed for HVI source classification and impact distance estimation; (3) the FCL algorithm is presented for accurate HVI source localization.

2 The proposed algorithm

2.1 SST features

To explicitly characterize the vibrations generated by HVI, we study the FSST and WSST and their advantages of good time-frequency resolution (Ghosh et al., 2019), strong robustness to white noise (Auger and Flandrin, 1995; Daubechies et al., 2011), and effective non-stationary signal description (Franco et al., 2012). Particularly, we focus on the vibrations generated by three different kinds of bullets in this study: (1) a lead projectile with a speed of 400 m/s (referred to as IMP1), (2) a steel projec-

tile with a speed of 900 m/s (referred to as IMP2), and (3) a polycarbonate projectile with a speed of 1000 m/s (referred to as IMP3). The sampling frequency of the vibration signal recording sensor is 5 kHz.

2.1.1 FSST features

The FSST feature extraction algorithm is summarized as follows:

For a vibration signal $x(n)$ of length N and parameter M:

Step 1: Use STFT to find the amplitude spectrum $\mathrm{STFT}^q(\omega)$ of vibration signal $x(n)$ using

$$\mathrm{STFT}^q(\omega) = \mathrm{STFT}[x(n)], \quad q = 1, 2, \ldots, M. \quad (1)$$

Step 2: According to the instantaneous frequency, calculate the rearranged spectrum $F^q(\omega)$ based on the SST as

$$F^q(\omega) = \mathrm{SST}[\mathrm{STFT}^q(\omega)], \quad q = 1, 2, \ldots, M. \quad (2)$$

Step 3: Calculate the energy distribution matrix $\boldsymbol{P}^q$ of $F^q(\omega)$ using

$$\boldsymbol{P}^q = \left[F^1(\omega), F^2(\omega), \ldots, F^M(\omega) \right]. \quad (3)$$

Step 4: Extract the FSST feature $\boldsymbol{P}_{\mathrm{FSST}}$ from the M frame data using

$$\boldsymbol{P}_{\mathrm{FSST}} = \left[P^1, P^2, \ldots, P^M \right]. \quad (4)$$

2.1.2 WSST features

The WSST feature extraction algorithm is summarized as follows:

For a vibration signal $x(n)$ of length N and parameter M:

Step 1: Use continuous wavelet transform (CWT) to find the amplitude spectrum $\mathrm{CWT}^q(\omega)$ of vibration signal $x(n)$:

$$\mathrm{CWT}^q(\omega) = \mathrm{CWT}[x(n)], \quad q = 1, 2, \ldots, M. \quad (5)$$

Step 2: According to the instantaneous frequency, calculate the rearranged spectrum $W^q(\omega)$ by the SST as

$$W^q(\omega) = \mathrm{SST}[\mathrm{CWT}^q(\omega)], \quad q = 1, 2, \ldots, M. \quad (6)$$

Step 3: Calculate the energy distribution matrix $\boldsymbol{P}^q$ of $W^q(\omega)$ as

$$\boldsymbol{P}^q = \left[W^1(\omega), W^2(\omega), \ldots, W^M(\omega) \right]. \quad (7)$$

Step 4: Extract the WSST feature $\boldsymbol{P}_{\mathrm{WSST}}$ from the M frame data using

$$\boldsymbol{P}_{\mathrm{WSST}} = \left[P^1, P^2, \ldots, P^M \right]. \qquad (8)$$

2.1.3 SST feature comparison

Figs. 2 and 3 show the comparisons of the WSST and FSST time-frequency diagrams obtained using the three different types of HVI sources and using the first HVI source (IMP1) collected at the three different distances to the sensor, respectively. As observed, WSST and FSST time-frequency diagrams have different distribution characteristics with different HVI sources and at different propagation distances. The coefficient size and distribution in the time-frequency diagram are important features, and would be applied to predict propagation distances and vibration sources.

For further analysis, we divide the frequency range into low, medium, and high subbands, and compare the spectrum percentages of each subband. As observed from Table 1, the percentage distributions of FSST and WSST characteristic coefficients with different vibration sources are basically consistent. Similar results can be obtained at different propagation distances, as shown in Table 2. When the propagation distance increases, the percentages of the medium and high subbands also increase for both FSST and WSST, and the increase is more obvious for FSST.

2.2 TCD features

GLCM is used to characterize texture distributions (Materka and Strzelecki, 1998; Mamli and
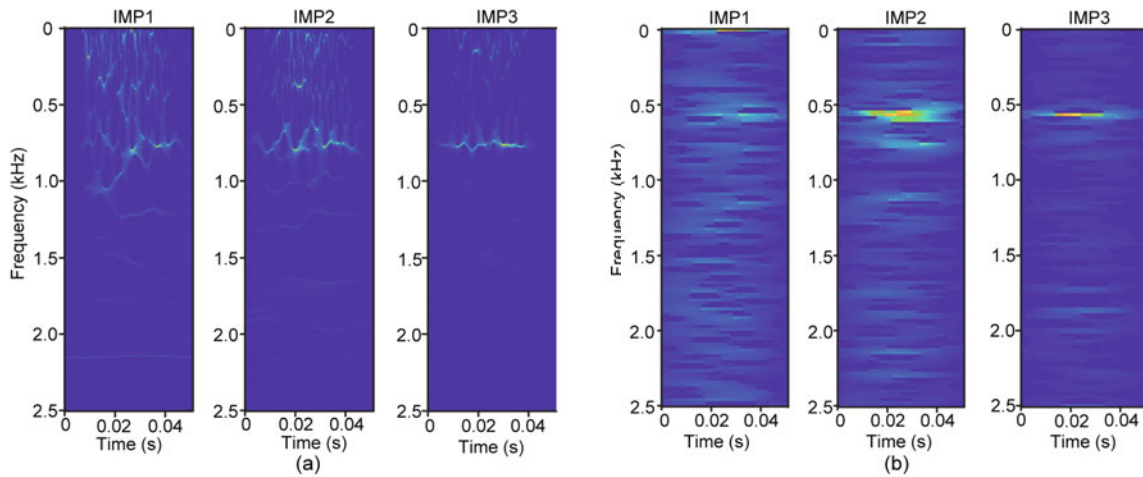

Fig. 2 WSST (a) and FSST (b) time-frequency diagrams of the three different types of HVI sources
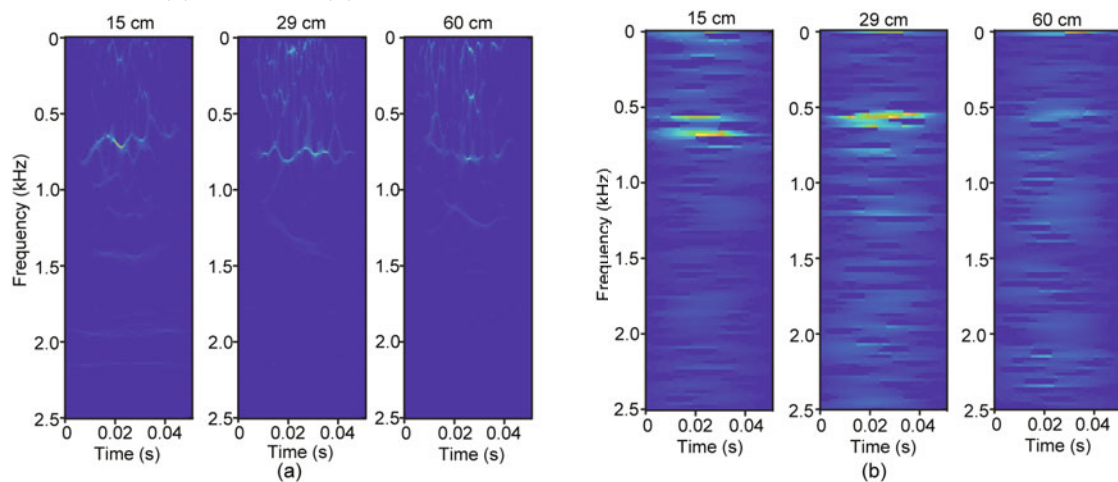

Fig. 3 WSST (a) and FSST (b) time-frequency diagrams of the first HVI source (IMP1) collected at three different distances to the sensor

Table 1 Percentage comparison of FSST and WSST coefficients with different HVI sources

Subband	Distribution percentage of FSST			Distribution percentage of WSST		
	IMP1	IMP2	IMP3	IMP1	IMP2	IMP3
Low	97.54%	92.23%	82.35%	98.08%	89.52%	79.46%
Medium	1.77%	5.85%	13.53%	1.52%	8.07%	16.84%
High	0.69%	1.92%	4.12%	0.40%	2.41%	3.70%

Table 2 Percentage comparison of FSST and WSST coefficients at different IMP1 propagation distances

Subband	Distribution percentage of FSST			Distribution percentage of WSST		
	15 cm	29 cm	60 cm	15 cm	29 cm	60 cm
Low	93.60%	57.20%	33.00%	97.51%	93.63%	89.33%
Medium	5.60%	33.00%	47.50%	1.81%	5.17%	8.00%
High	0.80%	9.80%	19.50%	0.68%	1.20%	2.67%

Kalbkhani, 2019) of the time-frequency spectrograms for HVI sources at different propagation distances. Four types of statistical indexes, including the correlation, energy, homogeneity, and entropy of four angles of the GLCM, are extracted. The three-channel entropy features (R, G, B) of the color time-frequency spectrogram image are also used for characterization.

GLCM characterizes the statistics of the spatial position and gray frequency of the pixels in the HVI signal time-frequency map, where d is the distance between the pixel (x, y) of image gray-level i and the pixel $(x + D_x, y + D_y)$ of image gray-level j. For the entire image, the number of occurrences of each type of (i, j) value is obtained and normalized to calculate the probability of occurrence $P(i, j, d, \theta)$ using

$$P(i, j, d, \theta) = \{(x, y), (x + D_x, y + D_y) | f(x, y) = i, \\ f(x + D_x, y + D_y) = j\},$$
(9)

where $i, j = 0, 1, \cdots, N - 1$ represent the grayscale and $N = 256$, d is the step size generated by the co-occurrence matrix, θ is the generation direction, and D_x and D_y are the position offsets, Finally, GLCM is obtained as an $N \times N$ square matrix. The correlation, energy, homogeneity, entropy on GLCM, and RGB global image entropy are extracted. Fig. 4 shows the pixel distribution of GLCM of the IMP1 source obtained at 15, 29, 60 cm.

With GLCM, TCDs of the FSST and WSST are extracted for HVI signals in detail in the following:

Step 1: extraction of gray-level images of the FSST and WSST time-frequency images

The RGB channels are set to a gray threshold to extract multiple channels of gray images. The texture features on different channels are calculated in the same way.

Step 2: gray level quantization

Normally, there are 256 gray levels in an image, from 0 to 255. To clearly reflect the clarity of the image, we divide it into 128 gray levels.

Step 3: parameter selection for calculating TCDs

The window size, distance to neighboring pixels, and directions in the gray level co-occurrence matrix are determined, which are set to be 7×7 pixels, 1 pixel, and $0°$, $45°$, $90°$, $135°$, respectively.

Step 4: calculation of texture feature values

The correlation, energy, homogeneity, and entropy of GLCM are calculated as texture features.

Step 5: calculation of global entropy of color images

The global image entropies of the RGB channels are calculated as the color features.

Step 6: composition of texture and color features

The texture and color features are composed as TCDs, a total dimension of 19.

The TCD features obtained from the FSST (TCD$_{\text{FSST}}$) and WSST (TCD$_{\text{WSST}}$) on the IMP1 HVI source at three different propagation distances to the sensor are compared in Tables 3 and 4, respectively. Overall, along with the increase of the propagation distance, for the same feature, the same trend can be observed in TCD$_{\text{FSST}}$ and TCD$_{\text{WSST}}$. For instance, the correlation decreases for both TCD$_{\text{FSST}}$ and TCD$_{\text{WSST}}$ when the propagation distance increases.
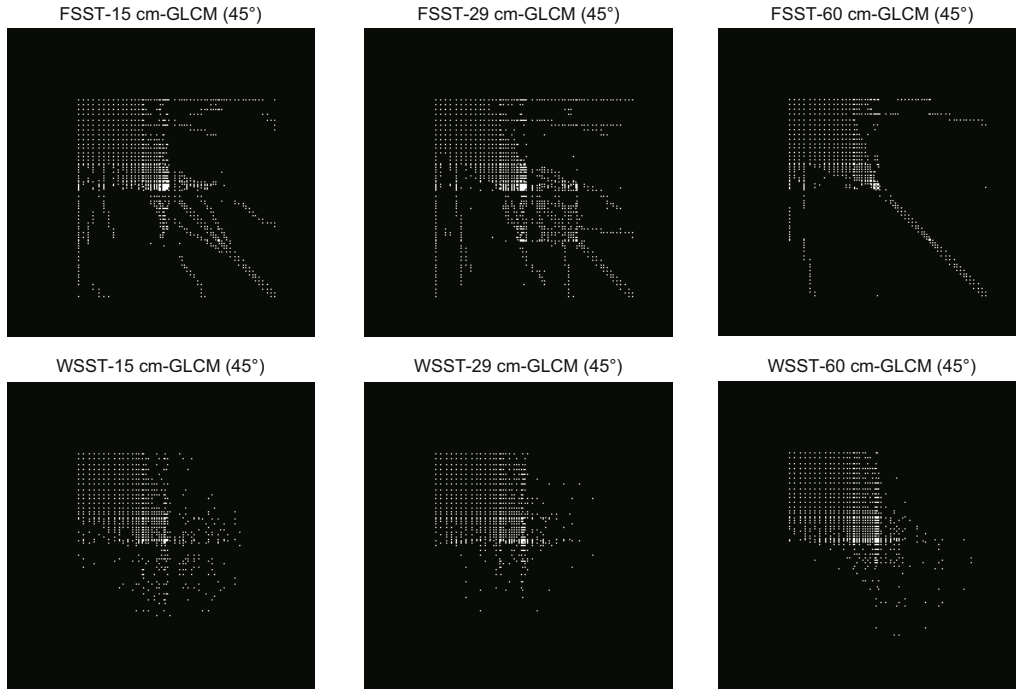
Fig. 4 Pixel distribution of the GLCM of IMP1 at different distances

Table 3 Analysis of TCD$_{\text{FSST}}$

Feature	TCD$_{\text{FSST}}$			Trend
	15 cm	29 cm	60 cm	
Correlation	0.978	0.973	0.959	Decrease
Energy	0.087	0.048	0.026	Decrease
Homogeneity	0.804	0.753	0.714	Decrease
Entropy (GLCM)	0.071	0.089	0.130	Increase
Global entropy (R)	3.267	3.536	4.076	Increase
Global entropy (G)	3.648	4.116	4.703	Increase
Global entropy (B)	3.615	4.053	4.553	Increase

Table 4 Analysis of TCD$_{\text{WSST}}$

Feature	TCD$_{\text{WSST}}$			Trend
	15 cm	29 cm	60 cm	
Correlation	0.938	0.933	0.924	Decrease
Energy	0.088	0.045	0.027	Decrease
Homogeneity	0.805	0.757	0.715	Decrease
Entropy (GLCM)	0.070	0.099	0.140	Increase
Global entropy (R)	3.157	3.456	4.176	Increase
Global entropy (G)	3.568	4.756	4.903	Increase
Global entropy (B)	3.745	4.803	4.953	Increase

2.3 HVI classification and distance estimation

Ensemble learning (Zhou, 2016) based on the majority voting strategy is applied for HVI source classification in this study, basically, as

$$
H(\boldsymbol{x}) = \begin{cases} c_j, & \text{if } \sum_{i=1}^{T} h_i^j(\boldsymbol{x}) > \\ & 0.5 \sum_{j=1}^{N} \sum_{i=1}^{T} h_i^j(\boldsymbol{x}), \\ \text{reject}, & \text{otherwise}, \end{cases}
\tag{10}
$$

where $i = 1, 2, \cdots, T$, $j = 1, 2, \cdots, N$, the N-dimensional vector $(h_i^1(\boldsymbol{x}), h_i^2(\boldsymbol{x}), \ldots, h_i^N(\boldsymbol{x}))$ is the predicted output of classifier h_i obtained on the feature sample $\boldsymbol{x}$, and $c_1, c_2, ..., c_N$ are the HVI source labels.

For the HVI propagation distance estimation, the stacked generalization strategy is adopted in ensemble learning to enhance the estimation performance. Particularly, the output of each individual estimator is stacked and used as the input to a final estimator to compute the propagation distance. This final estimator is trained through the cross-validation strategy. Fig. 5 shows the flowchart of the stacked generalization algorithm for HVI propagation distance estimation, and Algorithm 1 briefly summarizes the algorithm.

2.4 FCL algorithm

To accurately locate the vibration source, in this subsection we introduce the proposed FCL algorithm

Algorithm 1 Stacked generalization

1: The training set D is divided into m folders: $D = \{(x_1, y_1), (x_2, y_2), \ldots, (x_m, y_m)\}$ // training set
2: $\mathfrak{L}_1, \mathfrak{L}_2, \ldots, \mathfrak{L}_T$ // elementary learning algorithms
3: $\mathfrak{L}$ // secondary learning algorithm
4: **for** $t = 1, 2, \ldots, T$ **do**
5:     $h_t = \mathfrak{L}_t(D)$
6: **end for**
7: $D' = \varnothing$
8: **for** $i = 1, 2, \ldots, m$ **do**
9:     **for** $t = 1, 2, \ldots, T$ **do**
10:         $z_{it} = h_t(x_i)$
11:     **end for**
12:     $D' = D' \cup \{(z_{i1}, z_{i2}, \ldots, z_{iT}), y_i\}$
13: **end for**
14: $h' = \mathfrak{L}(D')$
15: $H(\boldsymbol{x}) = h'(h_1(\boldsymbol{x}), h_2(\boldsymbol{x}), \ldots, h_T(\boldsymbol{x}))$, where $\boldsymbol{x}$ is the feature sample
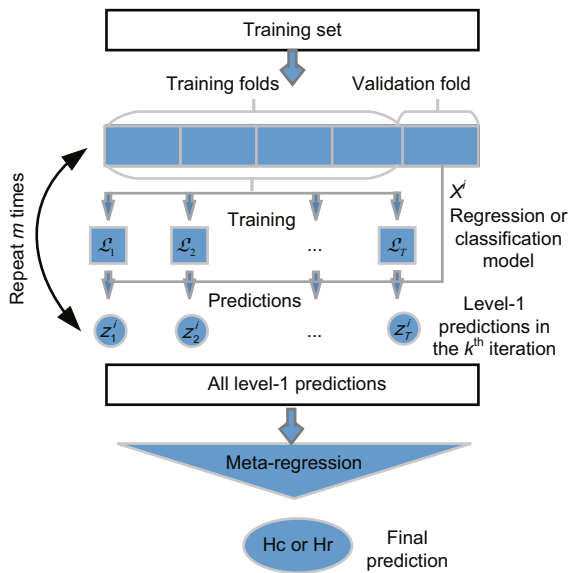16: Output: regression or classification model

---

Fig. 5 Stacked generalization algorithm

based on the propagation distance estimated by the previous stacking generalization model. We assume that all implemented sensors are capable of capturing vibrations, and that the vibration source is always within the effective detection range of the sensors. It is well known that in general, at least three non-collinear sensors are required to perform precise localization, for instance, the traditional three-circle centroid localization (TCL) algorithm (Shang et al., 2016; Cao et al., 2018). Ideally, if the propagation distance is accurately estimated, the source should be located at the intersection of the three circles, where their radii are the propagation distances d_1, d_2, and d_3, as shown in Fig. 6. However, due to the noise, measurement errors, and estimation biases, the TCL-based algorithm may not intersect at the same point. When there is a small error, as shown in Fig. 6, the actual coordinates of the vibration source are in the red region, and when the error is large, two circles do not intersect (Fig. 6b); it will lead to invalid localization by TCL. Consequently, we propose the accurate FCL algorithm, with the following detailed steps:

Step 1: When the center coordinates and radii of the four circles are known, it is easy to calculate the intersection of each two circles separately, and to obtain at most 12 intersection coordinates $[(x_1, y_1), \cdots, (x_n, y_n)], n = 2, 3, \ldots, 12$.

Step 2: According to the target size, the m ($m < n$) coordinates outside the effective plane are removed.

Step 3: Combine the remaining $n - m$ intersections to obtain C_{n-m}^3 red coordinate regions.
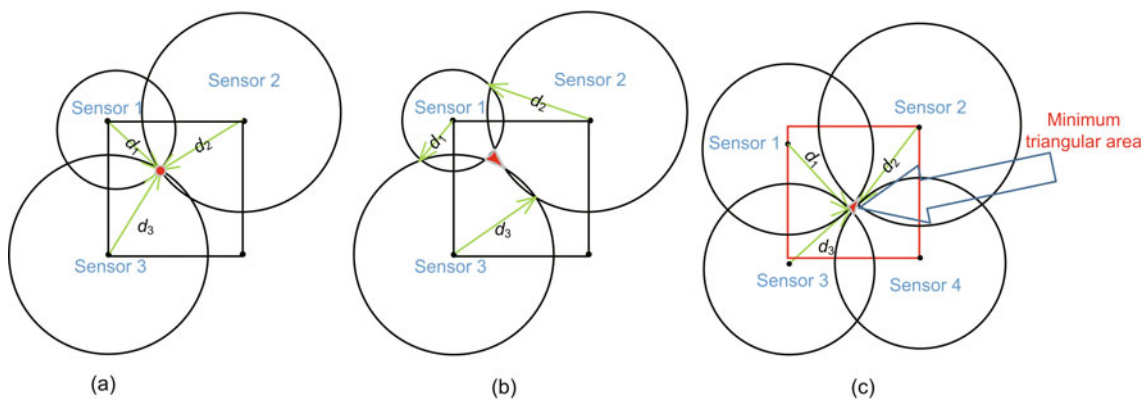
Step 4: Calculate the areas of the triangles

Fig. 6 HVI source localization comparison: (a) ideal localization; (b) localization with deviation; (c) localization with FCL (References to color refer to the online vesion of this figure)

determined by the three-point coordinates $\{S_1, S_2, \cdots, S_{n-2}\}$, and the area of the smallest triangle $S_{\min}$ is obtained. The actual intersection point is within the area of the triangle, as shown in Fig. 6c. The x and y coordinates of the three possible candidates are averaged as

$$(x, y) = \left(\frac{x_a + x_b + x_c}{3}, \frac{y_a + y_b + y_c}{3} \right), \quad (11)$$

where (x_i, y_i) $(i = a, b, c)$ are the three-point coordinates of $S_{\min}$, and (x, y) is the final estimated localization.

3 Experiments and discussions

3.1 Experimental setups

In this subsection, experiments on vibrations generated by the three different HVI sources were presented for performance validation. The three bullets were fired from a pistol, a 95-type automatic rifle, and a light gas gun (LGG), where the associated weights were 2, 4, and 0.38 g, respectively. The vibration signals were collected on an aluminum plate. For IMP1 and IMP2, the size of the aluminum plate was 700 mm × 700 mm × 3 mm (length×width×thickness), and for IMP3, the size was 300 mm × 300 mm × 3 mm. Four acceleration sensors, YD30 (https://www.zhendongsd.com/Product/detail/classid/13/id/71.html), were stuck on the four corners of the aluminum plate for vibration collection. The acquisition card type MCC1608G was used for signal recording. For each bullet, multiple tests were carried out; for IMP1 and IMP2, the experiments were performed in a shooting club in Hangzhou, China, and for IMP3, the vibration acquisition was conducted in HVI experiments on a hypervelocity-ballistic range at the China Aerodynamics Research and Development Center (CARDC), as shown in Figs. 7 and 8. There were 1824, 1788, and 5760 samples for the three impact sources, and for each sample, the frame length was set to be 256 points and the frame shift was 32 points. Because the bullets were randomly distributed on the aluminum plate, the recorded propagation distances to the sensor of the three bullets were separately within 15–87, 24–74, and 14–29 cm.

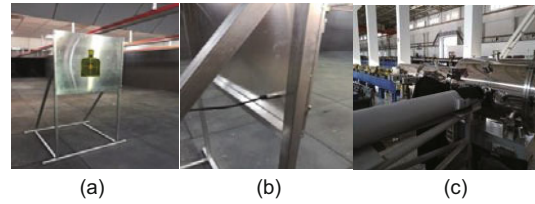**Fig. 7 Three types of bullets used in the experiments**

Fig. 8 Signal acquisition equipment (a), aluminum plate with a bullet hole (b), and vibration recording sensors (c)

3.2 HVI source classification

The comparison of the HVI source classification was shown in the first experiment based on the vibration signal, where the study focused mainly on using the FSST and WSST features. Comparison between the STFRFT and SPWVD vibration features was also presented, where the STFRFT and SPWVD time-frequency diagrams are shown in Figs. 9 and 10, respectively. The Hanning window was used for FSST and SPWVD with an order of 0.9. The experimental environment was based on the Python scikit-learn library.

Nine conventional popular classifiers, i.e., kNN, DT, SVM, LR, MLP, RF, ET, AdaBoost, and GB, were studied, where for the relevant hyperparameters of these algorithms, a grid search algorithm was used for optimization, and the optimal results were reported. In the experiment, 80% of data was randomly selected for model training, and the remaining 20% was used for testing. The root mean square error (RMSE) and determination coefficient R^2 were adopted as the regression model evaluation indicators, where R^2 is calculated as follows: $R^2 = 1 - \frac{\sum (y_a - y_p)^2}{\sum (y_a - y_m)^2}$. Here, y_a is the actual distance, y_p is the predicted distance, and y_m is the mean of all actual distances.

Table 5 shows the classification results of the three HVI sources (IMP1, IMP2, IMP3) based on
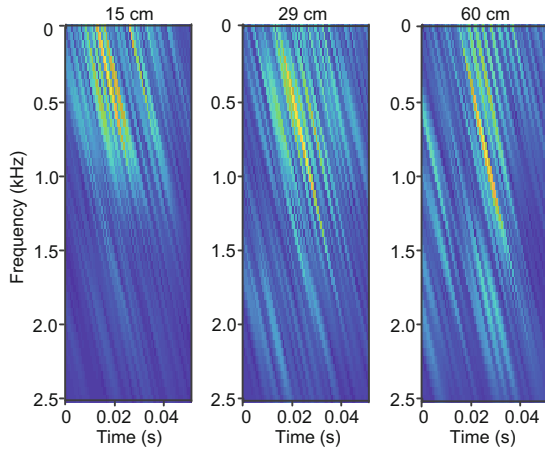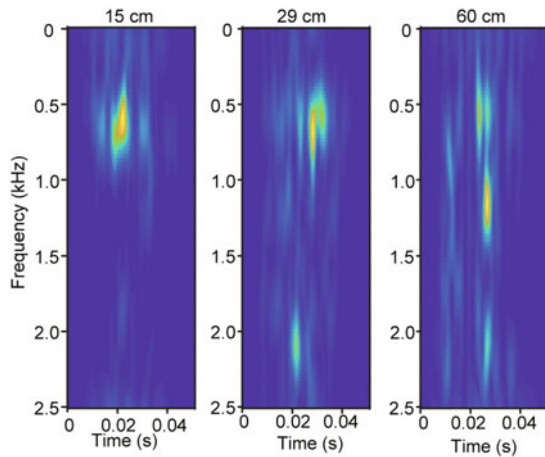
Fig. 9 STFRFT features

Fig. 10 SPWVD features

Table 5 HVI source classification comparison among conventional classifiers using FSST

Algorithm	Accuracy (%)
kNN	99.36
DT	91.47
SVM	98.72
LR	99.14
MLP	**99.57**
RF	98.50
ET	99.36
AdaBoost	93.60
GB	98.72

Best result is in bold

a single classifier and the FSST feature. It was observed that (1) all single classifiers can provide convincing classification performance for the HVI sources, where all accuracies are higher than 91%, and that (2) among all classifiers, MLP achieves the highest accuracy (99.57%). Therefore, we conclude that FSST is effective in characterizing HVI vibrations. The performance using the WSST features

was also tested and the same observations can be obtained, but the results are omitted here due to the space limitation.

The second experiment was based on the ensemble learning method for HVI source classification based on voting and stacking generalization strategies. Similar to the above experiment, only the results using the FSST feature are presented, whereas the WSST observations are omitted as similar performance can be obtained. For ensemble learning, three single classifiers were adopted as the basic module. For the voting strategy, all combinations of the seven conventional classifiers (kNN, DT, SVM, LR, MLP, ET, GB) were used, and therefore there were 35 classifier combinations (C_7^3). For stacked generalization, to reduce the risk of overfitting in model fusion, simple models such as kNN and LR were preferred. Therefore, we fixed the first model to either kNN or LR and tested the combination by the remaining classifiers (kNN, DT, SVM, LR, MLP, ET, GB). There were a total of 30 classifier combinations in stacked generalization.

Table 6 presents the HVI classification results of the voting-based ensemble learning model using FSST. From the table, one can see that (1) compared with the results using the single model in Table 5, ensemble learning with the voting strategy can provide more consistent and better accuracy, with the accuracy of almost all combinations being higher than 99%, but at the cost of higher computation complexity, and that (2) among all combinations, the accuracies of kNN+DT+GB and DT+MLP+GB are the highest, slightly higher than those of the other combinations. Table 7 shows the results using stacking generalization. As observed, (1) like the voting method, the stacking generalization based model can offer more consistent and better accuracy than a single classifier, and (2) compared with the voting strategy, stacking generalization performs slightly poorer on HVI source classification.

The last comparison in this subsection focused on the HVI source classification performance by the SST features (FSST and WSST), SPWVD, and STFRFT, where ensemble learning based on voting or stacking generalization was adopted. For all features, the classifier combination in the ensemble model with the best performance was reported. The classification accuracies given in Table 8 revealed that (1) SST features are more effective in HVI

source classification and that (2) the FSST-based model performs better than the WSST model.

3.3 HVI propagation distance estimation

Accurate estimation of the vibration propagation distance is a prerequisite for HVI source localization. In this subsection, we separately study the propagation distance estimation performances for these three different types of impact vibration signals. The performance obtained from the IMP1 HVI source using the FSST feature is discussed in detail and others are omitted due to similar observations. Table 9 shows the performance comparison of the eight single algorithms, revealing that AdaBoost is the most effective algorithm, with the RMSE and R^2 reaching 2.591 cm and 0.965, respectively.

Table 6 HVI source classification comparison using FSST with voting-based ensemble learning

Number	Model 1	Model 2	Model 3	Accuracy
1		DT	SVM	99.360%
2		DT	LR	99.147%
3		DT	MLP	99.360%
4		DT	ET	99.360%
5		DT	GB	**99.787%**
6		SVM	LR	99.360%
7		SVM	MLP	99.360%
8	kNN	SVM	ET	99.360%
9		SVM	GB	99.147%
10		LR	MLP	99.360%
11		LR	ET	99.360%
12		LR	GB	99.360%
13		MLP	ET	99.574%
14		MLP	GB	99.574%
15		ET	GB	99.360%
16		SVM	LR	99.147%
17		SVM	MLP	99.360%
18		SVM	ET	99.360%
19		SVM	GB	99.574%
20	DT	LR	MLP	99.147%
21		LR	ET	99.147%
22		LR	GB	99.574%
23		MLP	ET	99.574%
24		MLP	GB	**99.787%**
25		ET	GB	99.574%
26		LR	MLP	99.360%
27		LR	ET	99.360%
28	SVM	LR	GB	99.147%
29		MLP	GB	99.574%
30		MLP	ET	99.147%
31		ET	GB	98.934%
32		MLP	ET	99.574%
33	LR	MLP	GB	99.360%
34		ET	GB	99.147%
35	MLP	ET	GB	99.360%

Best results are in bold

The propagation distance estimation performances of the voting-based and stacking

Table 7 HVI source classification comparison using FSST with stacking generalization based ensemble learning

Number	Model 1	Model 2	Model 3	Accuracy
1		DT	SVM	98.507%
2		DT	LR	98.081%
3		DT	MLP	97.015%
4		DT	ET	99.147%
5		DT	GB	98.721%
6		SVM	LR	98.934%
7		SVM	MLP	98.934%
8	kNN	SVM	ET	98.934%
9		SVM	GB	98.721%
10		LR	MLP	92.324%
11		LR	ET	99.574%
12		LR	GB	99.360%
13		MLP	ET	99.574%
14		MLP	GB	99.574%
15		ET	GB	**99.787%**
16		DT	SVM	98.721%
17		DT	kNN	99.147%
18		DT	MLP	98.934%
19		DT	ET	99.360%
20		DT	GB	99.147%
21		SVM	kNN	99.147%
22		SVM	MLP	99.360%
23	LR	SVM	ET	99.360%
24		SVM	GB	98.934%
25		kNN	MLP	99.360%
26		kNN	ET	99.360%
27		kNN	GB	99.360%
28		MLP	ET	99.574%
29		MLP	GB	99.574%
30		ET	GB	99.574%

Best result is in bold

Table 8 HVI source classification comparison among FSST, WSST, SPWVD, and STFRFT features

Ensemble learning	Accuracy			
	FSST	WSST	SPWVD	STFRFT
Stacking	99.787%	98.934%	97.068%	97.174%
Voting	99.787%	98.987%	97.256%	97.482%

Table 9 HVI source propagation distance estimation comparison using FSST

Algorithm	RMSE (cm)	R^2
kNN	3.538	0.935
DT	8.576	0.619
SVM	10.681	0.409
MLP	4.568	0.891
RF	7.159	0.734
ET	4.307	0.903
AdaBoost	**2.591**	**0.965**
GB	5.140	0.863

Best results are in bold

generalization based ensemble learning algorithms are presented in Tables 10 and 11, respectively. Similarly, for voting, seven single classifiers were tested, leading to 35 combinations, and for stacking generalization, the first model adopted kNN and AdaBoost, leading to 30 combinations. From Tables 10 and 11, one can observe that (1) compared with the single model based HVI propagation distance estimation, ensemble learning with both the voting and stacking generalization strategies can generally provide relatively stable and accurate estimation performance, and that (2) for voting, the lowest RMSE and the highest R^2 were 3.054 cm and 0.952 respectively, and for stacking generalization, the lowest RMSE and the highest R^2 were 2.150 cm and 0.976 respectively, better than those of the voting-based strategy.

Comparison to existing vibration features, SP-WVD and STFRFT, with respect to propagation distance estimation, is given in Table 12, where results are reported for the three HVI sources. It can be seen from the table that: (1) SST features are more effective in HVI propagation distance estimation than SPWVD and STFRFT, (2) the FSST-based model performs better than the WSST-based model, and (3) when the velocity of the HVI source increases, the estimation performance is improved.

3.4 Distance estimation with optimized features

The main purpose of feature optimization in this subsection is to optimize the original features, reduce the feature dimension, improve the signal-to-noise

Table 10 Comparison of HVI source propagation distance estimation with voting-based ensemble learning

Number	Model 1	Model 2	Model 3	RMSE (cm)	R^2
1		DT	SVM	5.592	0.838
2		DT	AdaBoost	3.819	0.925
3		DT	MLP	4.344	0.902
4		DT	ET	4.446	0.898
5		DT	GB	4.991	0.871
6		SVM	AdaBoost	4.624	0.889
7		SVM	MLP	5.127	0.864
8	kNN	SVM	ET	5.117	0.864
9		SVM	GB	5.222	0.859
10		AdaBoost	MLP	**3.054**	**0.952**
11		AdaBoost	ET	3.062	0.951
12		AdaBoost	GB	3.228	0.946
13		MLP	ET	3.368	0.941
14		MLP	GB	3.514	0.936
15		ET	GB	3.820	0.924
16		SVM	AdaBoost	4.624	0.889
17		SVM	MLP	5.127	0.864
18		SVM	ET	5.117	0.864
19		SVM	GB	5.222	0.859
20		AdaBoost	MLP	**3.054**	**0.952**
21	DT	AdaBoost	ET	3.062	0.951
22		AdaBoost	GB	3.228	0.946
23		MLP	ET	3.368	0.941
24		MLP	GB	3.514	0.936
25		ET	GB	3.820	0.924
26		AdaBoost	MLP	**3.054**	**0.952**
27		AdaBoost	ET	3.062	0.951
28		AdaBoost	GB	3.228	0.946
29	SVM	MLP	GB	3.514	0.936
30		MLP	ET	3.368	0.941
31		ET	GB	3.820	0.924
32		MLP	ET	3.368	0.941
33	AdaBoost	MLP	GB	3.514	0.936
34		ET	GB	3.820	0.924
35	MLP	ET	GB	3.820	0.924

Best results are in bold

Table 11 Comparison of HVI source propagation distance estimation with stacking generalization based ensemble learning

Number	Model 1	Model 2	Model 3	RMSE (cm)	R^2
1		DT	SVM	8.596	0.618
2		DT	AdaBoost	4.519	0.894
3		DT	MLP	4.506	0.895
4		DT	ET	3.013	0.953
5		DT	GB	4.014	0.917
6		SVM	AdaBoost	5.510	0.843
7		SVM	MLP	4.210	0.908
8	kNN	SVM	ET	3.741	0.928
9		SVM	GB	4.521	0.894
10		AdaBoost	MLP	3.306	0.943
11		AdaBoost	ET	**2.150**	**0.976**
12		AdaBoost	GB	2.846	0.958
13		MLP	ET	3.698	0.929
14		MLP	GB	4.074	0.914
15		ET	GB	2.912	0.956
16		DT	SVM	7.980	0.670
17		DT	kNN	4.478	0.896
18		DT	MLP	4.945	0.873
19		DT	ET	3.293	0.944
20		DT	GB	4.394	0.900
21		SVM	kNN	4.874	0.877
22		SVM	MLP	4.210	0.908
23	AdaBoost	SVM	ET	3.741	0.928
24		SVM	GB	4.521	0.894
25		kNN	MLP	3.474	0.938
26		kNN	ET	2.312	0.972
27		kNN	GB	2.394	0.970
28		MLP	ET	3.698	0.929
29		MLP	GB	4.074	0.914
30		ET	GB	2.912	0.956

Best results are in bold

ratio, strengthen the anti-interference ability of the data, and further improve the localization accuracy. The essence of the propagation distance regression problem is to linearly fit the distance and the vibration signal feature. The better the fitting effect, the higher the degree of correlation and the greater the degree of similarity, indicating that the feature of this dimension is more discriminative. With this principle, we use the Pearson correlation coefficient ρ_{p}, Spearman correlation coefficient ρ_{s}, and cosine similarity $\cos(\theta)$ to measure the fitting effect. Then, the feature selection is performed based on thresholds of ρ_{p}, ρ_{s}, and $\cos(\theta)$.

$$\rho_{\mathrm{p}} = \frac{\sum_{i=1}^{N} x_i y_i - \frac{1}{N} \sum_{i=1}^{N} x_i \sum_{i=1}^{N} y_i}{\sqrt{\left(\sum_{i=1}^{N} x_i^2 - \frac{\left(\sum_{i=1}^{N} x_i\right)^2}{N}\right)\left(\sum_{i=1}^{N} y_i^2 - \frac{\left(\sum_{i=1}^{N} y_i\right)^2}{N}\right)}}, \tag{12}$$

Table 12 Propagation distance estimation comparison among the four features on IMP1, IMP2, and IMP3

HVI source	Ensemble learning	RMSE (cm)			
		FSST	WSST	SPWVD	STFRFT
IMP1	Stacking	2.150	2.380	9.30	7.74
	Voting	3.054	5.170	8.39	7.32
IMP2	Stacking	0.78	2.03	7.72	7.20
	Voting	1.54	3.76	6.71	6.23
IMP3	Stacking	0.26	0.32	1.38	1.11
	Voting	0.47	0.92	1.93	1.29

$$\rho_{\mathrm{s}} = \frac{\sum_{i=1}^{N} (x_i - \bar{x})(y_i - \bar{y})}{\sqrt{\sum_{i=1}^{N} (x_i - \bar{x})^2 \sum_{i=1}^{N} (y_i - \bar{y})^2}}, \tag{13}$$

$$\cos(\theta) = \frac{\sum_{i=1}^{N} x_i y_i}{\sqrt{\sum_{i=1}^{N} x_i^2} \sqrt{\sum_{i=1}^{N} y_i^2}}, \tag{14}$$

where $\boldsymbol{X} = [x_1, x_2, \cdots, x_N]$ and $\boldsymbol{Y} = [y_1, y_2, \cdots, y_N]$ are the labeled distance vector and the feature vector respectively.

Specifically, the normalized WSST and FSST features and their TCDs are stitched together (SST+TCD), and the obtained feature matrix is denoted as $\boldsymbol{T}_{m\times n}$. The propagation distances are denoted as a vector, $\boldsymbol{L}_{m\times 1}$.

The detailed feature optimization steps are summarized in the following:

Step 1: Calculate ρ_p, ρ_s, and $\cos(\theta)$.

Step 2: Determine the thresholds of ρ_p, ρ_s, and $\cos(\theta)$ for feature selection.

The thresholds are determined by a grid search parameter optimization method. With various combinations of ρ_p, ρ_s, and $\cos(\theta)$, a variety of different dimension fusion splicing features are calculated and the propagation distance regression RMSEs are calculated as the indicators. The threshold combination with a smaller RMSE is finally selected.

Step 3: Find the selected stitching feature.

The effective features y_j are finally selected.

Table 13 shows the propagation distance estimation comparison between the selected stitching features $\mathrm{OS_{SST+TCD}}$ and the original features SST+TCD, where dimensions of the selected features for IMP1, IMP2, and IMP3 were 215, 279, and 236 respectively, and the associated threshold values $(\rho_\mathrm{p}, \rho_\mathrm{s}, \cos(\theta))$ were $(0.005, 0.040, 0.600)$, $(0.005, 0.02, 0.650)$, and $(0.005, 0.01, 0.600)$, respectively. From the table, it was observed that the optimally selected feature can effectively improve the propagation distance estimation performance, compared with the original features for all the three HVI sources. In addition to accuracy enhancement, it has the advantages of eliminating redundant features and reducing the computational complexity.

3.5 HVI source localization

With the propagation distances estimated using multiple joint sensors, the coordinates of the HVI source were calculated by the proposed FCL algorithm. In this experiment, the distance mean square error D_MSE between the measured coordinates and the estimated ones was derived for performance evaluation, where D_MSE is defined as

$$D_\mathrm{MSE} = \frac{1}{n}\sum \sqrt{(X_n^\mathrm{p} - X_n^\mathrm{a})^2 + (Y_n^\mathrm{p} - Y_n^\mathrm{a})^2}, \quad (15)$$

where n is the number of samples, X^p and Y^p are the predicted x- and y-coordinate respectively, and X^a and Y^a are the actual x- and y-coordinate of the sample respectively.

Table 14 shows the D_MSE obtained by the conventional TCL algorithm and the proposed FCL method on IMP1, IMP2, and IMP3. It is apparent that the proposed FCL achieved a more consistently accurate localization than the conventional TCL method for all the three HVI sources.

4 Conclusions

Accurate hypervelocity impact (HVI) vibration source identification and localization play an important role in manned spacecraft protection, collision damage detection, and localization. In this paper, we have presented a novel HVI source classification, propagation distance estimation, and source localization algorithm. The Fourier and wavelet domain time-frequency spectrogram based synchrosqueezed transforms (SSTs) and their associated texture color distribution (TCD) have been proposed for HVI signal characterization. An optimal feature selection method based on the Pearson correlation coefficient, Spearman correlation coefficient, and cosine similarity has been developed for feature optimization. The HVI source classification, propagation distance estimation, and localization have been achieved by ensemble learning and a four-circle centroid

Table 14 HVI source localization comparison between TCL and the proposed FCL algorithm

Algorithm	D_MSE (cm)		
	IMP1	IMP2	IMP3
TCL	2.672	1.569	0.597
FCL	0.914	1.011	0.079

Table 13 HVI source propagation distance estimation comparison between the optimized features

Fusion feature	RMSE (cm)			R^2		
	IMP1	IMP2	IMP3	IMP1	IMP2	IMP3
SST+TCD	2.451	1.158	0.424	0.969	0.985	0.992
$\mathrm{OS_{SST+TCD}}$	1.670	1.009	0.264	0.986	0.988	0.996

localization algorithm. The effectiveness of the proposed algorithm has been demonstrated using real recorded HVI signals generated by three different high-speed bullets.

In this study, HVI source identification and localization have been used to accurately and effectively perform damage pattern recognition and evaluation. Specifically, we found that WSST and FSST features are highly efficient in characterization and discrimination. The improved vibration source identification and localization algorithm (SST, TCD+voting+stacking) achieves more accurate vibration source type recognition and improved distance prediction accuracy compared with the previous ones. Collision localization has been finally achieved using the distances estimated by multiple joint sensors, and the four-circle centroid localization algorithm further improves the accuracy of localization.

Contributors

Jiao BAO and Lifu LIU completed the experiments, processed the data, and drafted the paper. Jiuwen CAO designed the research, organized the paper, and revised and finalized the paper.

Compliance with ethics guidelines

Jiao BAO, Lifu LIU, and Jiuwen CAO declare that they have no conflict of interest.

References

Almeida LB, 1994. The fractional Fourier transform and time-frequency representations. *IEEE Trans Signal Process*, 42(11):3084-3091.
https://doi.org/10.1109/78.330368

Anderson JLB, Schultz PH, 2006. Flow-field center migration during vertical and oblique impacts. *Int J Impact Eng*, 33(1-12):35-44.
https://doi.org/10.1016/j.ijimpeng.2006.09.022

Auger F, Flandrin P, 1995. Improving the readability of time-frequency and time-scale representations by the reassignment method. *IEEE Trans Signal Process*, 43(5):1068-1089. https://doi.org/10.1109/78.382394

Bai X, Tao R, Liu LJ, et al., 2012. Autofocusing of SAR images using STFRFT-based preprocessing. *Electron Lett*, 48(25):1622-1624. https://doi.org/10.1049/el.2012.3169

Cao JW, Wang TL, Shang LM, et al., 2018. An intelligent propagation distance estimation algorithm based on fundamental frequency energy distribution for periodic vibration localization. *J Franklin Inst*, 355(4):1539-1558. https://doi.org/10.1016/j.jfranklin.2017.02.011

Cao JW, Zhang K, Yong HW, et al., 2019. Extreme learning machine with affine transformation inputs in an activation function. *IEEE Trans Neur Netw Learn Syst*, 30(7):2093-2107.
https://doi.org/10.1109/TNNLS.2018.2877468

Cao JW, Dai HZ, Lei BY, et al., 2020. Maximum correntropy criterion-based hierarchical one-class classification. *IEEE Trans Neur Netw Learn Syst*, 7:1-7.
https://doi.org/10.1109/TNNLS.2020.3015356

Chan HL, Huang HH, Lin JL, 2001. Time-frequency analysis of heart rate variability during transient segments. *Ann Biomed Eng*, 29(11):983-996.
https://doi.org/10.1114/1.1415525

Cohen L, 2013. leID1. Time-frequency analysis: theory and applications. *J Acoust Soc Am*, 134(5):4002.
https://doi.org/10.1121/1.4830599

Daubechies I, 1990. The wavelet transform, time-frequency localization and signal analysis. *IEEE Trans Inform Theory*, 36(5):961-1005.
https://doi.org/10.1109/18.57199

Daubechies I, Maes S, 1996. A nonlinear squeezing of the continuous wavelet transform based on auditory nerve models. In: Aldroubi A, Unser M (Eds.), Wavelets in Medicine and Biology. CRC-Press, Boca Raton, USA.

Daubechies I, Lu JF, Wu HT, 2011. Synchrosqueezed wavelet transforms: an empirical mode decomposition-like tool. *Appl Comput Harmon Anal*, 30(2):243-261.
https://doi.org/10.1016/j.acha.2010.08.002

Erickson AS, 2014. China's space development history: a comparison of the rocket and satellite sectors. *Acta Astronaut*, 103:142-167.
https://doi.org/10.1016/j.actaastro.2014.06.023

Flandrin P, Amin M, McLaughlin S, et al., 2013. Time-frequency analysis and applications. *IEEE Signal Process Mag*, 30(6):19-150.
https://doi.org/10.1109/MSP.2013.2270229

Franco C, Guméry PY, Vuillerme N, et al., 2012. Synchrosqueezing to investigate cardio-respiratory interactions within simulated volumetric signals. Proc 20th European Signal Processing Conf, p.939-943.

Ghosh SK, Tripathy RK, Ponnalagu RN, et al., 2019. Automated detection of heart valve disorders from the PCG signal using time-frequency magnitude and phase features. *IEEE Sens Lett*, 3(12):7002604.
https://doi.org/10.1109/LSENS.2019.2949170

Huang XG, Yin C, Huang J, et al., 2016. Hypervelocity impact of TiB$_2$-based composites as front bumpers for space shield applications. *Mater Des*, 97:473-482.
https://doi.org/10.1016/j.matdes.2016.02.126

Huang XG, Yin C, Ru HQ, et al., 2020. Hypervelocity impact damage behavior of B$_4$C/Al composite for MMOD shielding application. *Mater Des*, 186:108323.
https://doi.org/10.1016/j.matdes.2019.108323

Liou JC, Johnson NL, 2006. Risks in space from orbiting debris. *Science*, 311(5759):340-341.
https://doi.org/10.1126/science.1121337

Liu LF, Cao JW, Huang XG, 2019. High speed collision localization based on surface vibration processing. Proc 12th Int Symp on Computational Intelligence and Design, p.35-38.
https://doi.org/10.1109/ISCID.2019.10091

Mallat SG, 1989. Theory for multiresolution signal decomposition: the wavelet representation. *IEEE Trans Patt Anal Mach Intell*, 11(7):674-693.
https://doi.org/10.1109/34.192463

Mamli S, Kalbkhani H, 2019. Gray-level co-occurrence matrix of Fourier synchro-squeezed transform for epileptic seizure detection. *Biocybern Biomed Eng*, 39(1):87-99. https://doi.org/10.1016/j.bbe.2018.10.006

Materka A, Strzelecki M, 1998. Texture Analysis Methods—a Review. COST B11 Report. University of Lodz, Brussels, Belgium.

Millan RM, von Steiger R, Ariel M, 2019. Small satellites for space science: a cospar scientific roadmap. *Adv Space Res*, 64(8):1466-1517. https://doi.org/10.1016/j.asr.2019.07.035

Mirzapour F, Ghassemian H, 2013. Using GLCM and Gabor filters for classification of PAN images. 21st Iranian Conf on Electrical Engineering, p.1-6.

Monti A, Medigue C, Mangin L, 2002. Instantaneous parameter estimation in cardiovascular time series by harmonic and time-frequency analysis. *IEEE Trans Biomed Eng*, 49(12):1547-1556. https://doi.org/10.1109/TBME.2002.805478

Önsay T, Haddow AG, 1993. Comparison of STFT, Gabor, and wavelet transforms in transient vibration analysis of mechanical systems. *J Acoust Soc Am*, 93(4):2290. https://doi.org/10.1121/1.406528

Pierazzo E, Melosh HJ, 2000. Hydrocode modeling of oblique impacts: the fate of the projectile. *Meteorit Planet Sci*, 35(1):117-130. https://doi.org/10.1111/j.1945-5100.2000.tb01979.x

Qian SE, Chen DP, 1999. Joint time-frequency analysis. *IEEE Signal Process Mag*, 16(2):52-67. https://doi.org/10.1109/79.752051

Shang LM, Cao JW, Wang JZ, et al., 2016. Fundamental frequency energy distribution of periodic vibrations and their relation to distance. Proc IEEE 13th Int Conf on Signal Processing, p.96-101. https://doi.org/10.1109/ICSP.2016.7877804

Stankovic L, Stankovic S, Dakovic M, 2014. From the STFT to the Wigner distribution. *IEEE Signal Process Mag*, 31(3):163-174. https://doi.org/10.1109/MSP.2014.2301791

Tao R, Li YL, Wang Y, 2010. Short-time fractional Fourier transform and its applications. *IEEE Trans Signal Process*, 58(5):2568-2580. https://doi.org/10.1109/TSP.2009.2028095

Thakur G, Brevdo E, Fučkar NS, et al., 2013. The synchrosqueezing algorithm for time-varying spectral analysis: robustness properties and new paleoclimate applications. *Signal Process*, 93(5):1079-1094. https://doi.org/10.1016/j.sigpro.2012.11.029

Torrence C, Compo G, 1998. A practical guide to wavelet analysis. *Bull Amer Meteorol Soc*, 79(79):61-78.

Wang TL, Cao JW, Lai XP, et al., 2020. Hierarchical one-class classifier with within-class scatter-based autoencoders. *IEEE Trans Neur Netw Learn Syst*, 32(8):3770-3776. https://doi.org/10.1109/TNNLS.2020.3015860

Wilson EK, 2019. Space tourism moves closer to lift off. *Engineering*, 5(5):819-821. https://doi.org/10.1016/j.eng.2019.08.006

Witze A, 2018. The quest to conquer Earth's space junk problem. *Nature*, 561(7721):24-26. https://doi.org/10.1038/D41586-018-06170-1

Yang MQ, Kpalma K, Ronsin J, 2008. A survey of shape feature extraction techniques. *Patt Recogn*, 15(7):43-90.

Yin C, Xue T, Huang XG, et al., 2019. Research on damages evaluation method with multi-objective feature extraction optimization scheme for M/OD impact risk assessment. *IEEE Access*, 7:98530-98545. https://doi.org/10.1109/ACCESS.2019.2930114

Zhou ZH, 2016. Machine Learning. Tsinghua University Press, Beijing, China (in Chinese).